IOP Publishing Smart Materials and Structures

Smart Mater. Struct. **23** (2014) 025030 (12pp) doi:10.1088/0964-1726/23/2/025030

Control of a piezoelectrically actuated high-speed serial-kinematic AFM nanopositioner

Sachin P Wadikhaye[1], Yuen Kuan Yong[1], Bharath Bhikkaji[2] and S O Reza Moheimani[1]

[1] School of Electrical Engineering and Computer Science, University of Newcastle, Callaghan, NSW, Australia
[2] Department of Electrical Engineering, Indian Institute of Technology Madras, Chennai, India

E-mail: reza.moheimani@newcastle.edu.au

Received 5 August 2013, revised 11 December 2013
Accepted for publication 12 December 2013
Published 9 January 2014

Abstract

Controller design to compensate vibration, hysteresis and time delay in a high-speed serial-kinematic X–Y nanopositioner is presented in this paper. A high-speed serial-kinematic X–Y nanopositioner, designed in-house, is installed in a commercial AFM and its scanning performance is studied. The impediments to fast scanning are (i) the presence of mechanical resonances in the nanopositioning stage, (ii) nonlinearities due to the piezoelectric actuators and (iii) time delay introduced by finite clock speeds of the signal conditioning circuitry associated with displacement sensors. In this paper an integral resonant controller is designed to mitigate the effect of the resonance along the X axis (fast axis). The control design accommodates for the time delay, thereby ensuring robust stability. A high gain integral controller is wrapped around the damped nanopositioner to ensure sufficient linearity near the region of operation. For actuation along the Y axis (slow axis), where the bandwidth requirement is less demanding, a notch filter is used to increase the gain margin and the nonlinearity is compensated using a high gain feedback controller. Enhancement in the scanning speed up to 200 Hz is observed. Imaging and tracking performance for open loop and closed loop scans up to 200 Hz line rate is compared and presented. Limitations and future work are discussed.

Keywords: high-speed atomic force microscope (AFM), flexure guided nanopositioner, piezoelectric actuators, integral resonant control (IRC), time delay, tracking

(Some figures may appear in colour only in the online journal)

1. Introduction

The atomic force microscope (AFM) was first introduced in 1986 by Binnig and Quate [1] to develop the surface topology of non-conducting samples with atomic resolution. Since its invention, the AFM has become one of the most versatile scientific instruments, with its applications extended in many scientific fields such as physics [2], chemistry [3], biology [4], material science [5], metrology [6], and more. Advancement and research in the field of nanotechnology such as the work reported in [7] have been possible with the help of the AFM. Applications of the AFM have been growing and researchers in many fields are attempting to customize AFMs as per their requirements [8–10]. One such requirement is a high-speed AFM which allows the visualization of biological processes that occur within a fraction of a second [11–15].

The AFM generates three dimensional images of a sample surface using the positioning information along its three axes. In practice, the sample is moved in a raster pattern with the help of a nanopositioner to achieve lateral positioning. The sample surface is probed to deduce the vertical positioning information corresponding to the lateral

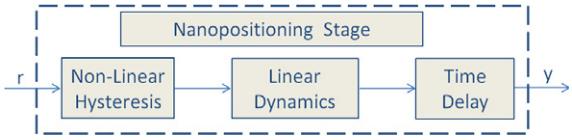

Figure 1. Different components of the nanopositioning stage model.

position of the sample. Raster scanning involves actuating one of the axes of the nanopositioner to track a triangular signal. A triangular signal contains all odd harmonics of its fundamental frequency [16]. The higher harmonics constitute the edges of triangular signals which are responsible for sharp changes in the direction of motion of the nanopositioning stage. While tracking a triangular signal, these harmonics may excite the structural resonances, leading to vibrations that hamper tracking of signals. Therefore, the scanning frequency, in practice, is limited to one tenth of the structural resonance frequency [17–19]. High-speed nanopositioning applications require positioners with high resonance frequencies. This enables the actuators to change the direction of motion of the nanopositioning stage at high scanning rates without triggering the resonances of the stage. Most commercial AFMs are equipped with piezoelectric tube nanopositioners. The scanning bandwidth of a typical nanopositioner is limited to a few Hertz because of its low resonance frequency. Recently, flexure-guided nanopositioners have been used as an alternative to piezoelectric tube nanopositioners [9, 20–24]. Flexure-based nanopositioners produce smooth motion through elastic deformation of a structure. They can be designed to have significantly higher resonance frequencies than those of piezoelectric tube nanopositioners.

Although a higher resonance frequency can be achieved by efficient mechanical design of flexure-based nanopositioners, the tracking performance is limited due to their lightly damped structure. Also, flexure-based nanopositioners incorporate piezoelectric actuators [9, 12, 25, 23, 21, 26, 27] which show nonlinear behavior like hysteresis and creep [17–19]. Capacitive sensors are often used in nanopositioning applications because of their high resolution and bandwidth. The sensor readout circuit introduces a time delay in the system, which deteriorates the tracking performance. Figure 1 shows that the main impediments to performing high-speed scanning are vibrations, nonlinearities and time delay. In this paper, we attempt to address these three issues in order to achieve high-speed scanning with nanoscale accuracy.

To overcome nonlinearities and for effective tracking of reference signals, closed loop tracking controllers often incorporate a high gain integral action [18, 19]. The controller provides high gain at low frequencies and effectively reduces the effect of nonlinearities. However, the presence of lightly damped resonance poles imposes restrictions on gain margins, limiting the bandwidth of the controller. Damping of resonant peaks is an effective method to increase the bandwidth of the integral control. Different damping techniques have been reported in the literature such as positive position feedback (PPF) [28], shunt control [29], resonant control [30], integral resonant control (IRC) [31–34] and, more recently, force feedback control [35]. Inversion-based controllers such as inversion filters [36] have also been reported which use inverted plant dynamics to suppress the resonant peaks. However, inversion-based controllers do not provide robustness to changes in system parameters which is critical in nanopositioning systems. The load mass in these systems changes with the investigated sample causing significant variation in the natural frequencies of the system. On the other hand, damping controllers artificially increase the damping of the closed loop system making it comparatively insensitive to changes in natural frequencies and, thus, facilitate the robust implementation of integral controllers for tracking.

In this paper, IRC was designed and implemented in closed loop on a high-speed nanopositioning stage to damp the first resonant mode of the stage. Integral resonant control has been recently introduced [37] as a simple, robust and high-performance control technique for damping resonant modes of flexible structures with collocated piezoelectric actuator–sensor pairs. It has been successfully used to control the vibrations of manipulator arms [38] and piezoelectric tubes [34]. Other controllers, such as loop shaping controllers and optimal controllers such as LQG, have been implemented to improve scanning performance [39–43]. However, they typically lead to controllers with orders that could be several times larger than that of the plant [41]. The sliding mode control approach has also been investigated as a control design tool for robust tracking in nanopositioning systems [44–46].

It has been shown in [34, 47] that, in the positive feedback configuration, IRC provides guaranteed closed loop stability for negative imaginary systems under some finite gain conditions. These results are not always applicable to all high-speed nanopositioning systems as they are often not negative imaginary. For example, the time delay introduced by the signal conditioning circuitry of the capacitive sensors becomes significant over the large bandwidth of the nanopositioning system. Consequently, they should be treated as a resonant system with a time delay. In this paper, the stability conditions for IRC are evaluated to accommodate resonant time delayed systems such as nanopositioning stages using the framework of the results presented in [48].

The Smith predictor has been shown to compensate the effects of time delay in plants [49]. The working of the Smith predictor, however, is based on the internal model control (IMC) principle which is not suitable in the current context. The IMC principle involves inverting the plant dynamics for cancellation of poles, in this case the lightly damped poles. The robustness of the closed loop with respect to perturbations in system parameters is not guaranteed with IMC. This may lead to degradation in tracking performance and non-repeatability of scans.

In the case of high bandwidth nanopositioners the effect of time delay can be seen in the tracking performance in the form of phase lag. Feedforward control integrated with feedback control can be used to overcome the delay [50, 51]. Direct inversion of plant dynamics is not possible as the time delay introduces non-minimum phase (NMP) zeros in the system. Inversion of such a system will lead to unstable poles.

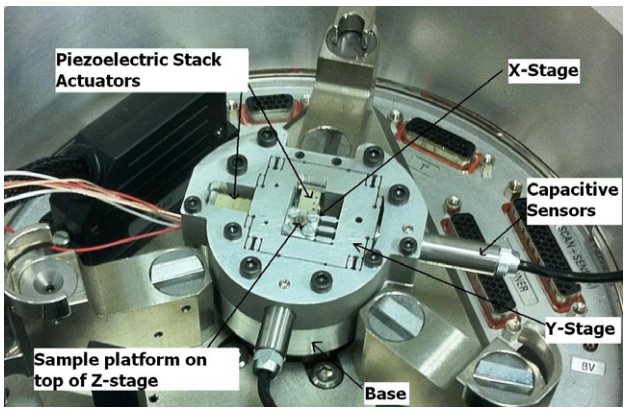

Figure 2. High-speed X–Y nanopositioner.

In this paper, off-line inversion of the plant dynamics has been presented which uses Fourier series to construct the input to the plant [32].

The paper is organized as follows. Section 2 describes briefly the nanopositioner used for experimentation. In section 3, characterization of the nanopositioner dynamics is presented and models are identified for control design. Section 4 presents the design of IRC for the X-stage. Feedforward control is presented in section 5 followed by discussion on the design of the notch filter and high gain feedback linearization for the Y-stage in section 6. Section 7 describes the setup used for experiments. Comparison of the imaging performance of a nanopositioner installed in a commercial AFM in open and closed loop is presented in section 8. Section 9 concludes the paper.

2. High-speed nanopositioner

As stated earlier, a piezoelectric tube nanopositioner typically has low resonance frequency which limits the scanning speed to a few hertz. For example, the piezoelectric tube nanopositioner presented in [34] has a resonance frequency of 840 Hz; thus, the scanning bandwidth is limited to around 8.5 Hz. It would take half a minute to scan an image of 256 × 256 pixel resolution. The processes occurring within a fraction of a second require much higher scanning speeds. One would not be able to extract adequate information about a sample with fast dynamics from images generated with a scan speed of 8.5 Hz. Flexure-based nanopositioners has been shown to have much higher scanning speeds than piezoelectric tube nanopositioners [20, 9, 25, 23, 21]. To design a compact flexure-based nanopositioner which would replace an existing piezoelectric tube nanopositioner in an AFM is a difficult task. Manufacturing constraints and machining tolerances imposed on the design (such as smallest available tool on the market) make the design process for a compact scanner even more challenging.

Figure 2 shows a compact serial-kinematic nanopositioner designed in-house to replace a piezoelectric tube nanopositioner installed in an NT-MDT NTEGRA AFM. The nanopositioner is designed such that its maximum diameter is 45 mm and it can be installed in the space available for the piezoelectric tube nanopositioner. The detailed design and characterization of this compact high-speed nanopositioner has been reported in [24, 27]. The Y-stage is built large to accommodate the X-stage such that its operation is not affected by the dynamics of the X-stage. To make the nanopositioner compact, the X-stage is built with a fixed–free arrangement [52] with flexures on one side of the stage. Aluminum-7075 is used for manufacture of the nanopositioner because of its high yield strength to weight ratio [53, 23]. The nanopositioner is manufactured using wire electro discharge machining (WEDM). To actuate the X and Y stages with high acceleration, Noliac (SCMAP07 5 mm × 5 mm × 10 mm) piezoelectric stack actuators are used. The Z-stage is built on the X-stage using a piezoelectric stack actuator (Noliac SCMAP06 3 mm × 3 mm × 4 mm), which is placed in a cavity on the X-stage. A plate flexure is designed for the Z-stage to achieve a natural frequency of 100 kHz and is screwed on top of the piezoelectric stack actuator. The travel ranges for the nanopositioner are 8 μm and 5 μm along the x and y directions respectively. The natural frequency of the stage along the x-direction is 9.6 kHz and along the y-direction is 7 kHz.

3. Identification

In this section, the experimental characterization of the nanopositioner dynamics is presented. The nanopositioner is interpreted as a linear system with two inputs and two outputs $Y(s) = G(s)U(s)$, where $U(s)$ denotes the Laplace transform of $[v_X, v_Y]^\top$, the voltage signals applied to the electrodes of the piezoelectric stacks along the x and y directions, $Y(s)$ denotes the Laplace transform of $[d_X, d_Y]^\top$ and

$$G(s) = \begin{bmatrix} G_{XX}(s) & G_{XY}(s) \\ G_{YX}(s) & G_{YY}(s) \end{bmatrix}, \tag{1}$$

the transfer function relating the inputs and the outputs.

To identify the linear models of these transfer functions, small signal frequency response functions (FRFs) are estimated. It should be noted that at small amplitudes the nonlinear effects such as hysteresis can be considered negligible. In figures 3(a) and (b), the magnitude and phase responses of the individual FRFs of $G(\mathrm{i}\omega)$ are plotted in blue. These FRFs were determined using an HP35670A dual channel spectrum analyzer. A swept sine input of 50 mVpk with a frequency range of 10 Hz to 20 kHz was applied to drive the piezoelectric stack actuators along the X and Y axes and the corresponding capacitive sensor responses were recorded. Individual FRFs were computed by taking the Fourier transform of the recorded data.

It is apparent from the plots that the nanopositioner has a resonance at 6.05×10^4 rads s^{-1} (i.e., 9.62 kHz) along the X axis and at 4.43×10^4 rads s^{-1} (i.e., 7.07 kHz) along the Y axis. In addition to the resonant behavior, the phase response appears to include a linear term (see the dotted line in figure 3(b)), suggesting a time delay. In other words, the phase plots suggest that the transfer-function matrix is of the form $G(s)\mathrm{e}^{-s\tau}$ for some time delay $\tau > 0$, with $G(s)$

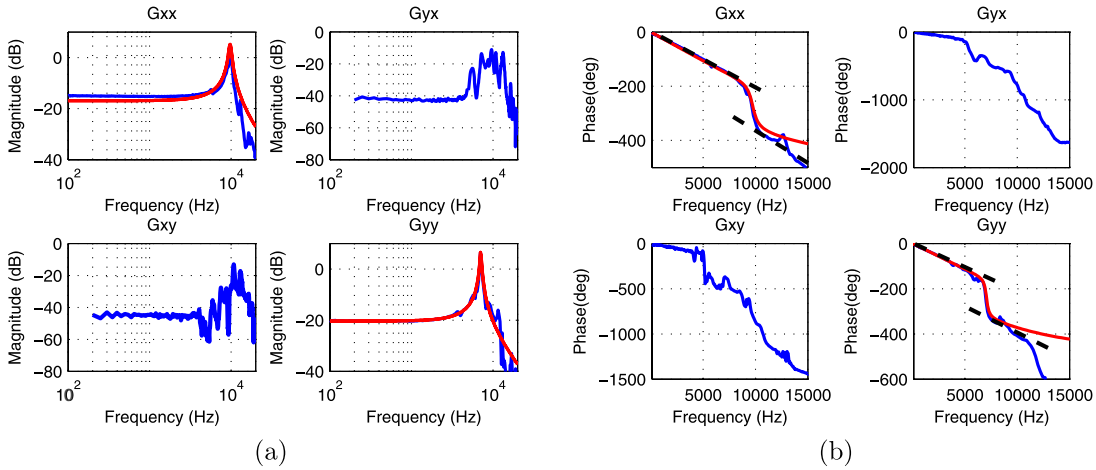

Figure 3. (a) Magnitude responses of the FRFs relating the inputs and outputs. (b) Phase responses of the FRFs relating the inputs and outputs (on linear scale). Plots in blue are the open loop responses and the plots in red represent the system identified with time delay.

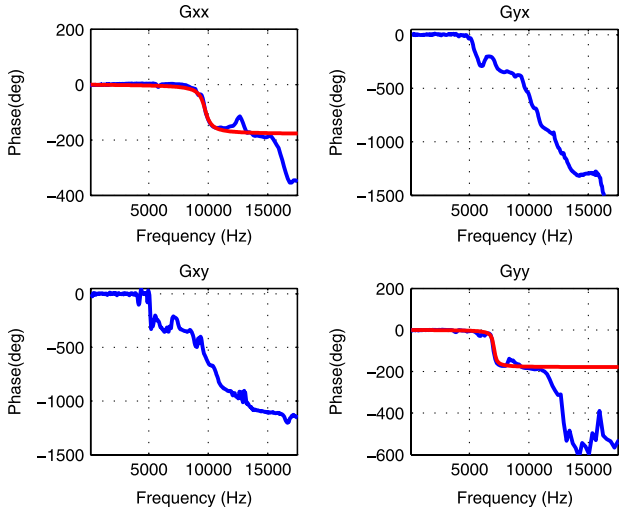

Figure 4. Phase responses of the FRFs relating the inputs and outputs. Plots in blue are the open loop responses and plots in red represent the system identified without the time delay.

denoting a highly resonant finite order system. Figure 4 shows the phase response of the resonant component. This plot is generated by estimating the time delay τ, which was found to be approximately 62 μs, and multiplying the individual FRF data by $e^{i\omega\tau}$. Note that the time delay τ is the slope of the dotted straight line in figure 3(b).

For controller design, only the diagonal terms $G_{XX}(s)$ and $G_{YY}(s)$ of (1) are considered. The cross coupling terms $G_{XY}(s)$ and $G_{YX}(s)$ are neglected. It is apparent from the dashed–dotted plots in figures 3(a) and 4 that the resonant parts of $G_{XX}(s)$ and $G_{YY}(s)$ can be satisfactorily modeled as second order systems. The following models were estimated for the resonant transfer functions using the sub-space method [54]:

$$G_{XX}(s) = \frac{5.33 \times 10^8}{s^2 + 4800s + 3.743 \times 10^9}, \tag{2}$$

Table 1. Hysteresis measurements for the X- and Y-stages.

Axis	Max. width (μm)	Disp. range (μm)	%
X	2.2	6.4	34
Y	1.2	4.1	29

$$G_{YY}(s) = \frac{1.897 \times 10^8}{s^2 + 1978s + 1.972 \times 10^9}. \tag{3}$$

In figures 3(a) and 4 the magnitude and phase responses of the models (2) and (3) respectively are plotted with red lines. A good fit can be observed. As the system also includes a time delay $\tau = 62$ μs, the transfer functions $G_{XX}(s)$ and $G_{YY}(s)$ are multiplied by

$$T(s) = \frac{s^2 - 9.231 \times 10^4 s + 2.84 \times 10^9}{s^2 + 9.231 \times 10^4 s + 2.84 \times 10^9}, \tag{4}$$

which is a second order Pade approximation of $e^{-s\tau}$. Figure 4 shows the phase responses of the transfer functions $G_{XX}(s)T(s)$ and $G_{YY}(s)T(s)$. The plots suggest that the models fit the respective data sets with reasonable accuracy.

One of the disadvantages of using piezoelectric stack actuators is the inherent nonlinearity due to hysteresis [19]. To study the effect of hysteresis a 10 Hz triangular wave of 200 V is applied to the X and Y axis actuators of the nanopositioner. The response of the system is measured and plotted against the input signals to generate the hysteresis loops as plotted in figure 5. To quantify the hysteresis the maximum width of the hysteresis curve is taken as the parameter expressed as the percentage of the full range along the respective axis. Table 1 illustrates the amount of hysteresis along the X and Y axes.

4. IRC control design for the fast stage

In this paper an integral resonant controller (IRC) is designed to damp the resonant modes. In [37, 34], IRCs have been designed for damping resonant systems. Here, the IRC design

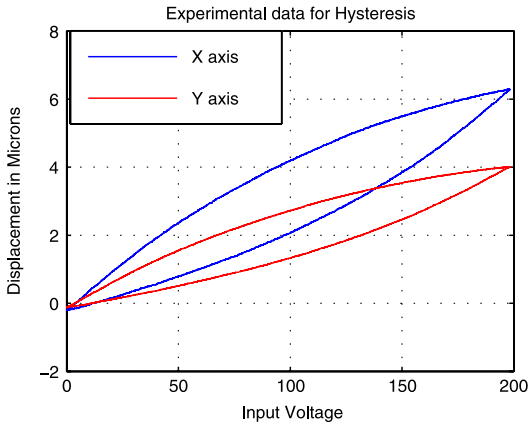

Figure 5. Plots showing the hysteresis loop obtained by plotting the input voltage versus the output displacement along the X and Y axes.

procedure is extended to accommodate systems with time delay. In the following a controller will be designed to damp the resonant mode of $G_{XX}(s)T(s)$.

An IRC controller has the following structure:

$$C(s) = \frac{K}{s - Kd}, \tag{5}$$

with $K > 0$ and $d < 0$. The reasons for setting $d < 0$ will become apparent soon. Direct calculations would reveal that the imaginary part of $C(\mathrm{i}\omega)$ is also strictly negative for $\omega > 0$. Note that positive feedback connection of $G_{XX}(s)$ and $C(s)$ leads to a closed loop transfer function

$$\begin{aligned} G_{\mathrm{cl}}(s) &\triangleq \frac{G_{XX}(s)\frac{K}{s-Kd}}{1 - G_{XX}(s)\frac{K}{s-Kd}} \\ &= \frac{G_{XX}(s)K}{(s - Kd - KG_{XX}(s))} \\ &= \frac{G_{XX}(s)\frac{K}{s}}{\left(1 - (G_{XX}(s) + d)\frac{K}{s}\right)}. \end{aligned} \tag{6}$$

Since the denominator of (6) is

$$R(s) = \left(1 - (G_{XX}(s) + d)\frac{K}{s}\right), \tag{7}$$

by setting d to be equal to any suitable negative real number and varying K, one can formulate a root locus type procedure to determine a set of closed loop poles, which are zeros of (7), that impart good damping.

This procedure was used in [37, 34]. However, for the root locus plot to be lying complexly in the left half plane, both $G_{XX}(s)$ and $C(s)$ have to be strictly negative imaginary and $G(0)C(0) < 1$ [34]. Note that $G_{XX}(s)$ described in equation (2) has a frequency response with an imaginary part that is negative for all $\omega > 0$,

$$G_{XX}(\mathrm{i}\omega) = \frac{5.33 \times 10^8 \left(3.743 \times 10^9 - \omega^2 - \mathrm{i}4800\omega\right)}{\left(3.743 \times 10^9 - \omega^2\right)^2 + (4800\omega)^2}. \tag{8}$$

Here, the system that is to be controlled is $G_{XX}(s)T(s)$, which is not negative imaginary. In figure 6(a), a Nyquist plot of $G_{XX}(s)T(s)$ is presented. It can be inferred that $G_{XX}(s)T(s)$ is negative imaginary in the intervals $[0, \omega_1]$ and $[\omega_2, \infty)$, where $\omega_1 = 5.04 \times 10^4$ rads s^{-1} and $\omega_2 = 6.69 \times 10^4$ rad s^{-1}. Meanwhile, in the interval $[\omega_1, \omega_2]$ the system is not negative imaginary. Therefore results pertaining to strictly negative imaginary systems [55] cannot be applied.

In figure 6(b), a Nyquist plot of $-G_{XX}(\mathrm{i}\omega)T(\mathrm{i}\omega)$ is presented. Note that $-G_{XX}(\mathrm{i}\omega)T(\mathrm{i}\omega)$ is negative imaginary between $[\omega_1, \omega_2]$, while it is bounded by a circle of radius $k_1 = 0.67$ in the frequency regions $[0, \omega_1]$ and $[\omega_2, \infty)$. In a recent publication [48], stability results corresponding to systems that are negative imaginary in certain frequency regions and have 'small' gain in other intervals have been presented. It has been shown in [48] that, if a controller $C(s)$ is strictly negative imaginary and the plant $G(s)$ violates the negative imaginary property over certain intervals, say $[\omega_k, \omega_{k+1}]$, for $k = 1, 2, \ldots, N$, then the closed loop is stable in positive feedback configuration if the following conditions are met.

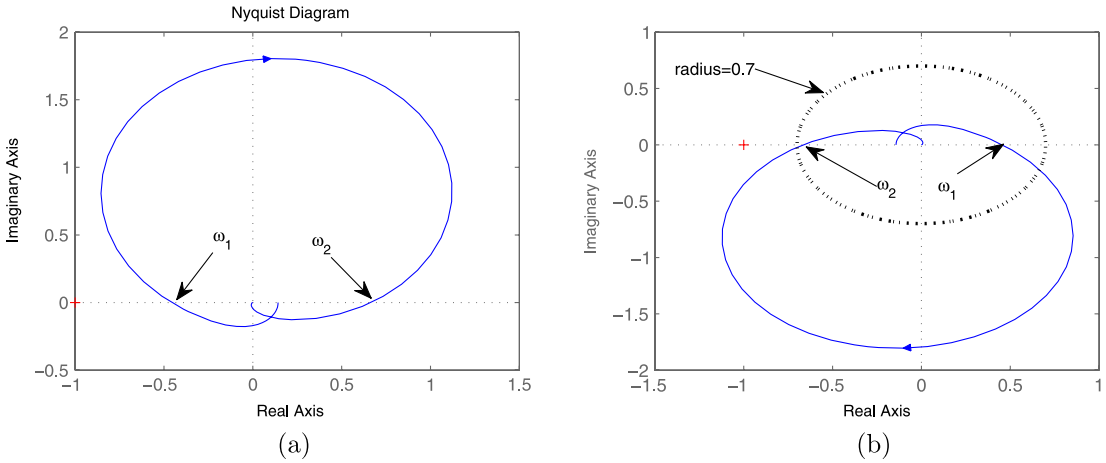

Figure 6. (a) Nyquist plot of $G_{XX}(\mathrm{i}\omega)T(\mathrm{i}\omega)$. (b) Nyquist plot of $-G_{XX}(\mathrm{i}\omega)T(\mathrm{i}\omega)$, along with a circle (dotted) of radius -0.7.

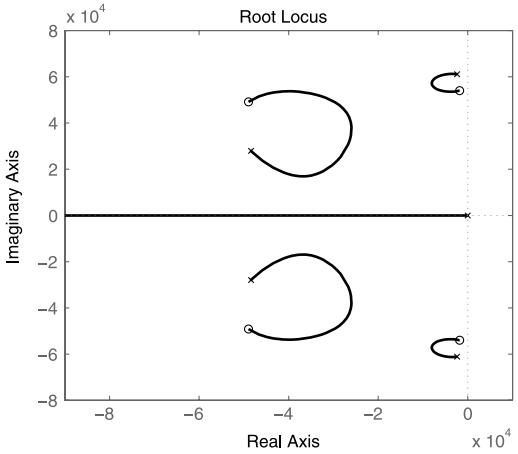

Figure 7. Root locus of $R(s)$, obtained by varying $K \geq 0$ with $d = -0.7$.

(i) $\lim_{s\to\infty} G(s)C(s) = 0$.

(ii) There exist constants K_1 and K_2 such that $|G(0)| < K_1$, $|C(0)| < K_2$ and $K_1K_2 < 1$.

(iii) In the intervals $[\omega_k, \omega_{k+1}]$ for $k = 1, 2, \ldots$ where $G(\mathrm{i}\omega)$ is not negative imaginary both $G(\mathrm{i}\omega)$ and $C(\mathrm{i}\omega)$ must be bounded, i.e., $|G(\mathrm{i}\omega)| < K_1$ and $|C(\mathrm{i}\omega)| < K_2$ for all $\omega \in [\omega_k, \omega_{k+1}]$, for $k = 1, 2, \ldots$.

Note that for an IRC controller

$$\max_{\omega} |C(\mathrm{i}\omega)| = C(0) = \frac{-1}{d}, \tag{9}$$

which implies $|d| > \frac{1}{k_2} > k_1 = 0.67$. Therefore, $|d|$ has to be greater than 0.67. Here, we set $d = -0.7$, and plot the root locus for

$$R(s) \triangleq \left(1 - (-G_{XX}(s)T(s) + d)\frac{K}{s}\right), \tag{10}$$

by varying K, see figure 7. From the root locus plot, we choose $K = 3.2 \times 10^4$, which implies that

$$C(s) = \frac{3.2 \times 10^4}{s + 3.2 \times 0.7 \times 10^4}. \tag{11}$$

In figure 8 the closed loop frequency response function, with the above mentioned controller, is presented by a green line. It is apparent from the plots that significant damping of the resonances has been achieved for the chosen controller.

As mentioned earlier, an integral controller with gain $K = 32\,000$ has been implemented and the closed loop frequency response with the integral controller has been plotted with a red line in figure 8.

5. Feedforward control for the fast stage

A brief explanation of inversion-based feedforward techniques is presented in this section. An extensive review on feedforward techniques is presented in [50]. The goal of any inversion technique is to find the input u such that when fed to a linear system with known dynamics G_{XX}, it produces the

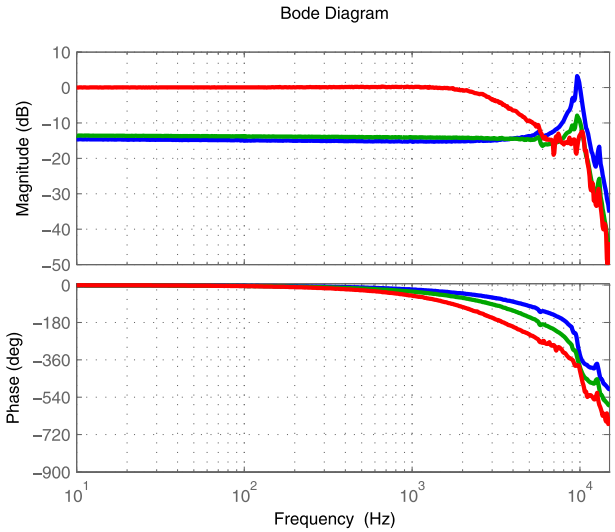

Figure 8. Frequency response for the X-stage. The plot in blue shows the open loop response, the plot in green shows the response of closed loop with IRC and the plot in red shows the closed loop response with IRC+Integrator.

desired output y_d [31, 50, 18]. In other words, it is desirable to acquire a u such that

$$Y_d(\mathrm{i}\omega) = G_{XX}(\mathrm{i}\omega)U(\mathrm{i}\omega), \tag{12}$$

where $U(\mathrm{i}\omega)$ and $Y_d(\mathrm{i}\omega)$ are Fourier transforms of u and the desired trajectory y_d respectively.

Direct inversion of plant dynamics is one of the methods to achieve the feedforward control. This is a straightforward technique where the system identified from the frequency response function is inverted. In most cases, where the bandwidth is not large, the time delay can be neglected. However, in the case of high-speed nanopositioning where the structural resonance is greater than 1 kHz, the phase drop due to time delay is significant. In such cases G_{XX} will have non-minimum phase (NMP) zeros. Inversion of such a system will result in an unstable system. If the time delay is neglected in the inversion, the higher harmonics will be shifted by a certain phase dictated by the time delay. Thus, the inversion will not lead to the input u that produces the desired output y_d.

A simpler and more effective approach is to construct the input signals from Fourier series. During raster scans, the fast stage of the nanopositioner tries to track a triangular signal. The desired output of the stage is a triangular signal which in Fourier series form can be written as

$$y_d(t) = \sum_{k=1}^{\infty} A_k \sin(\omega_k t), \tag{13}$$

where $A_k = \frac{8}{\pi^2 k^2}\sin(\frac{\pi k}{2})$ and $\omega_k = 2\pi kf$, with f being the fundamental frequency of the triangular waveform. Thus, in order to obtain the desired output $y_d(t)$, the input should be

$$u(t) = \sum_{k=1}^{\infty} \frac{A_k}{|G_{XX}(\mathrm{i}\omega_k)|}\sin(\omega_k t - \phi_k), \tag{14}$$

where $\phi_k = \angle G_{XX}(\mathrm{i}\omega_k)$ and $k = 1, 2, \ldots$.

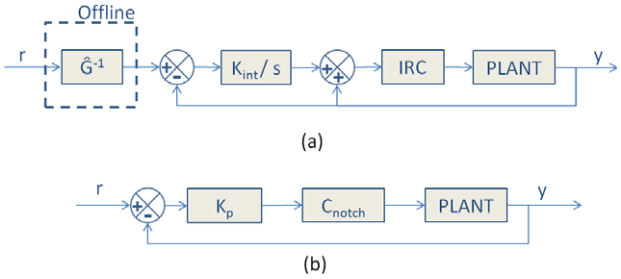

Figure 9. (a) Control strategy for X-stage, (b) control strategy for Y-stage.

Here, the desired trajectory $y_d(t)$, and hence $u(t)$, has an infinite number of harmonics and is consequently not band-limited. If the harmonics are limited to the frequencies before resonance is reached, a precise inversion can be achieved and would ease the inversion process. Also, if the harmonic content in the inversion bandwidth of the reference signal is limited, the sensitivity to modeling error can be reduced [56]. Thus, equation (14) can be rewritten as

$$u(t) = \sum_{k=1}^{n} \frac{A_k}{|G_{XX}(\mathrm{i}\omega_k)|} \sin(\omega_k t - \phi_k), \tag{15}$$

where n is the number of odd harmonics to be tracked. By using this technique the original phase ϕ_k calculated from the FRF is used to construct the input signal $u(t)$.

It is shown in [57] that to achieve a scan speed of up to 10% of the resonance frequency, the number of harmonics should be limited to nine or less. With nine harmonics, one can achieve approximately 70% of the linear scan range. Figure 8 shows that, for the fast stage of the nanopositioner, the resonance is at 10 kHz with a tracking bandwidth of up to 5 kHz. Hence, a triangular signal with a fundamental frequency of up to 500 Hz with nine odd harmonics can be approximated.

It is evident from figure 8 that the phase drop up to the tracking bandwidth of 5 kHz is significant. By constructing a feedforward input to the plant using equation (15) harmonics of the fundamental frequency with the original phase and magnitude are incorporated. Thus, an exact inverse of the plant for the required harmonics can be implemented. Figure 9(a) shows the control strategy for the X-stage.

6. High gain feedback linearization of hysteresis for the slow stage

For a serial-kinematic nanopositioner the slow stage (the Y-stage) tracks a slowly increasing ramp. The bandwidth requirement here is $2n$ times less than that of the fast stage, where n is the number of scan lines. For the slow stage a high gain feedback control is sufficient to overcome the effects of nonlinearities. However, the resonant modes with low structural damping (or high quality factor) impose low gain margins which restrict the application of higher gain in the closed loop [51]. Low gains are in some cases insufficient to improve the tracking performance of the system.

The resonant behavior of the slow stage can be sufficiently suppressed by implementing a notch filter. Suppression of resonant peaks increases the gain margins and hence the tracking performance can be improved over the bandwidth of interest. The structure of the notch filter is of the form

$$C_{\text{notch}} = \frac{s^2 + \frac{d}{c}\omega_n + \omega_n^2}{s^2 + \frac{1}{c}\omega_n + \omega_n^2}, \tag{16}$$

where ω_n is the resonance frequency of the Y-stage, and the coefficients d and c can be iterated to suppress the effect of dominant resonant peaks. The coefficients d and c were chosen to be 0.022 and 0.5 respectively. The resonance frequency ω_n was calculated from the FRF as 4.44×10^4 rad sec^{-1}. Figure 10 shows that the gain margin was

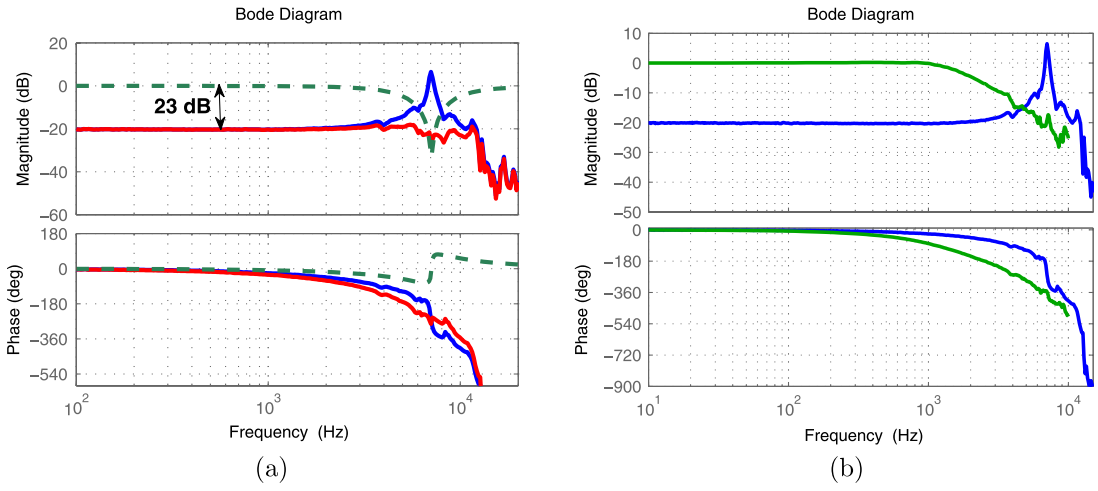

Figure 10. (a) Open loop frequency response for the Y-stage in blue; the green dashed plot represents the notch filter and the open loop response of C_{notch} + Plant is shown in red. A gain margin of 23 dB is indicated which is obtained after cascading the notch filter with the stage. (b) Open loop frequency response for the Y-stage in blue; a closed loop Proportional + C_{notch} + Plant is shown in green.

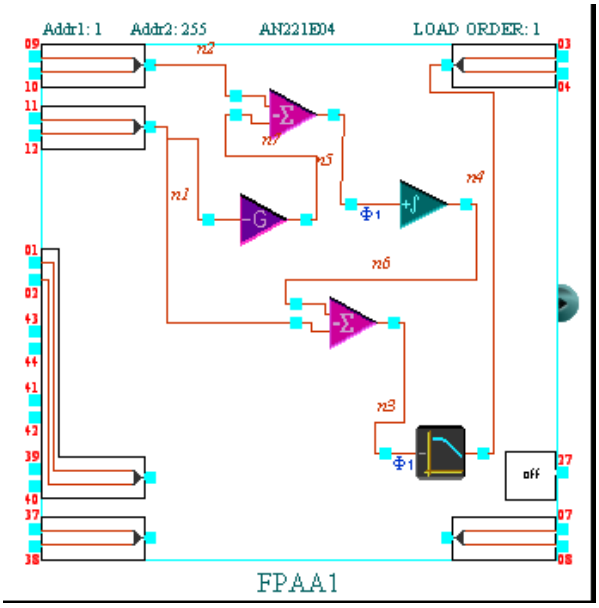

Figure 11. FPAA implementation of the control strategy.

improved from 0.007 to 23 dB. The notch filter along with a high gain feedback of $K_p = 20\,000$ was realized using Matlab Simulink and a dSPACE rapid prototyping system, as shown in figure 9(b). Figure 10(b) shows the open loop and closed loop frequency responses which indicate a 0 dB magnitude response for frequencies up to 1 kHz.

7. Experimental setup

In this section, the implementation of the control scheme presented in the previous sections is discussed. The nanopositioner was installed in an NT-MDT NTEGRA AFM and was used to test the proposed control strategy. Three piezoelectric stack actuators were used to actuate the stage at high acceleration with large force. Noliac SCMAP07 (5 mm $\times$ 5 mm $\times$ 10 mm, 380 nF) piezoelectric stack actuators were used to actuate the X- and Y-stages, while a Noliac SCMAP06 (3 mm $\times$ 3 mm $\times$ 4 mm, 35 nF) was used to drive the Z-stage. PiezoDrive PDL 200 external voltage amplifiers were used to drive the piezoelectric stacks, each with a gain of 20. Two ADE Technologies 8810/2804 capacitive sensors, with a gain of 2.5 μm V^{-1}, were used to measure the displacement of the stage in the x and y directions.

The data acquisition system of the commercial NT-MDT NTEGRA SPM used in the experiments has a limitation on sampling rate. The maximum scan rate achievable is 31 Hz for a 256 $\times$ 256 pixel resolution image. The scan rate can be increased to a higher value but at the cost of the resolution,

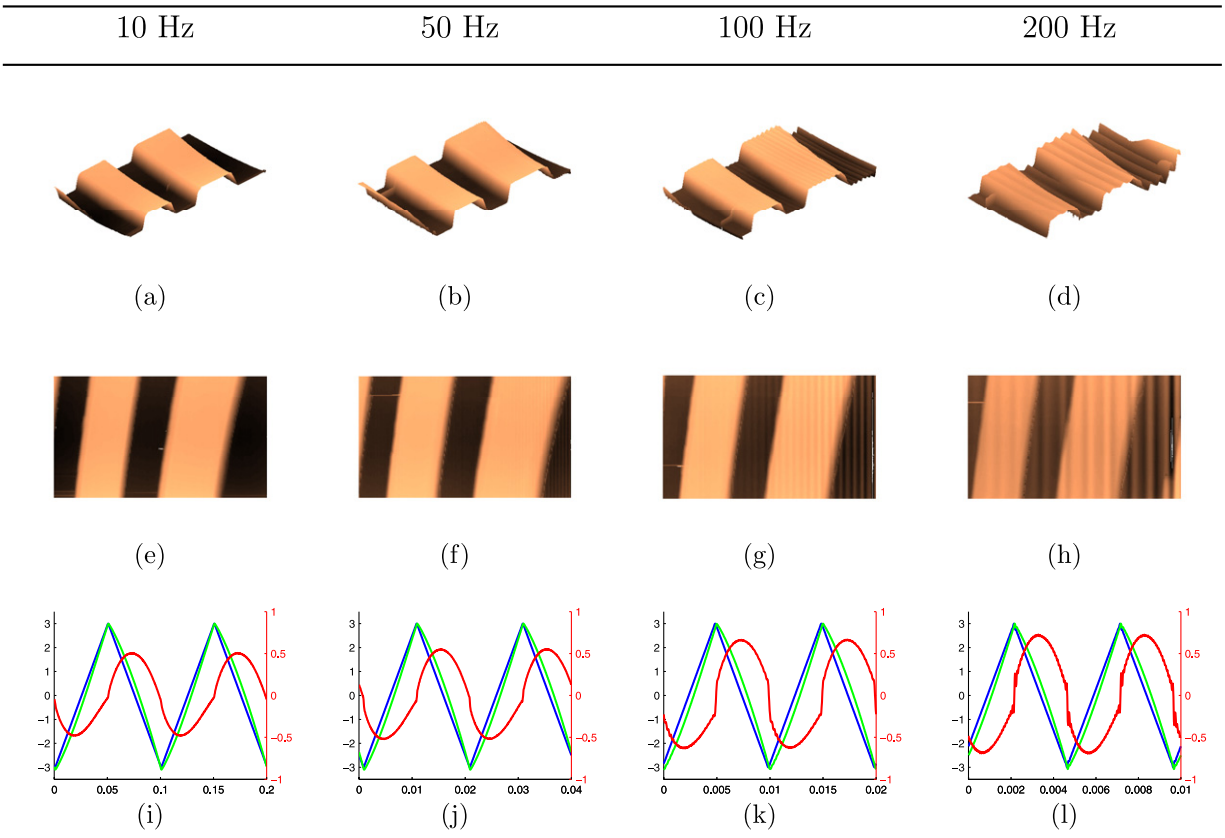

Figure 12. Open loop scan performance of the nanopositioner for the scanning speed indicated at the top: blue lines represent the reference signal, green lines indicate the output signals from the capacitive sensors converted to equivalent displacement and red lines represent the tracking error.

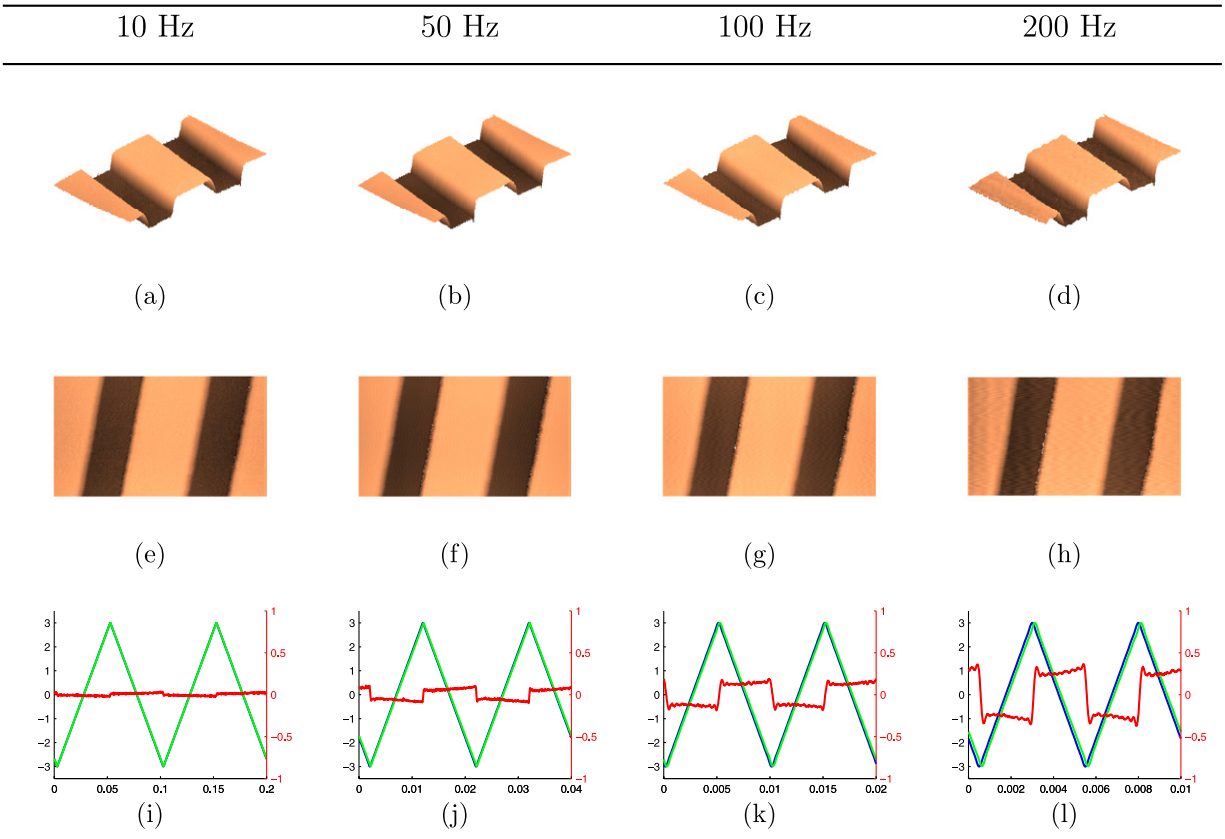

Figure 13. Closed loop scan performance without feedforward of the nanopositioner: blue lines represent the reference signal, green lines indicate the output signals from the capacitive sensors converted to equivalent displacement and red lines represent the tracking error.

e.g. the scan rate can be increased to 62 Hz with a decrease in resolution to 128 × 128 pixels. To overcome this limitation a dSPACE-1103 rapid prototyping system is used with 80 kHz sampling rate. With this system scan rates up to 200 Hz can be reached with a resolution of 200 × 200 pixels.

Also, the sampling rate provided by the rapid prototyping system is insufficient for implementing the high bandwidth controller in equation (11). The IRC scheme along with the integral action was implemented using a field programmable analog array (FPAA). The controller was realized on a commercially available Anadigm Vortex (AN221K04) FPAA development board. The FPAA is an integrated device which contains interconnected configurable analog blocks (CABs). These CABs can be used to configure analog circuits such as filters. They consist of OPAMP circuitry with switching capacitors which makes it possible to achieve switching frequencies of around 15 MHz, eliminating the sampling and quantization effects. Figure 11 shows a schematic of the *X*-stage control implementation presented in figure 9(a) on FPAA boards using Anadigm-2 software. The in-built functions of Bilinear Filter, Integrator, Inverse Gain and Inverse Sum were used to develop the controller. The control strategy for the *Y*-stage shown in figure 9(b) was implemented using a dSPACE rapid prototyping system and Matlab/Simulink.

Images were obtained using the constant height contact mode of the AFM.

8. Imaging and tracking performance

In this section the performance of the designed nanopositioner is evaluated by installing it in the AFM and performing high-speed scans. A MikroMasch TGZ01 calibration grating was scanned. This grating has step features of 3 μm period and 200 nm height. Images with a 6 μm × 4 μm scan size with a pixel resolution of 200 × 200 were recorded at 10 Hz, 50 Hz, 100 Hz, and 200 Hz scan rates. Scanned images for open loop, closed loop and closed loop with feedforward control are shown in figures 12, 13 and 14 respectively.

Figure 12 shows the open loop scans of the calibration grating. Oscillations due to harmonics of the triangular signals and the resonance frequency can be observed distinctly at 100 Hz. At 200 Hz these oscillations are increased which severely deteriorates the image. The difference in the feature size can be observed in figures 12(e) to (h); these discrepancies in the images are due to the presence of hysteresis. The severity of hysteresis and oscillations is evident from the *x*-direction signal plots shown in figures 12(i) to (l).

Significant reduction in the oscillations and hysteresis can be observed in figure 13 after implementing the controller in closed loop along the X and Y axes. It is evident from figures 13(a) to (d) that oscillations are suppressed by the IRC. The high controller gain reduces the distortions due to hysteresis significantly, see figures 13(e) to (h). Figures 13(i)

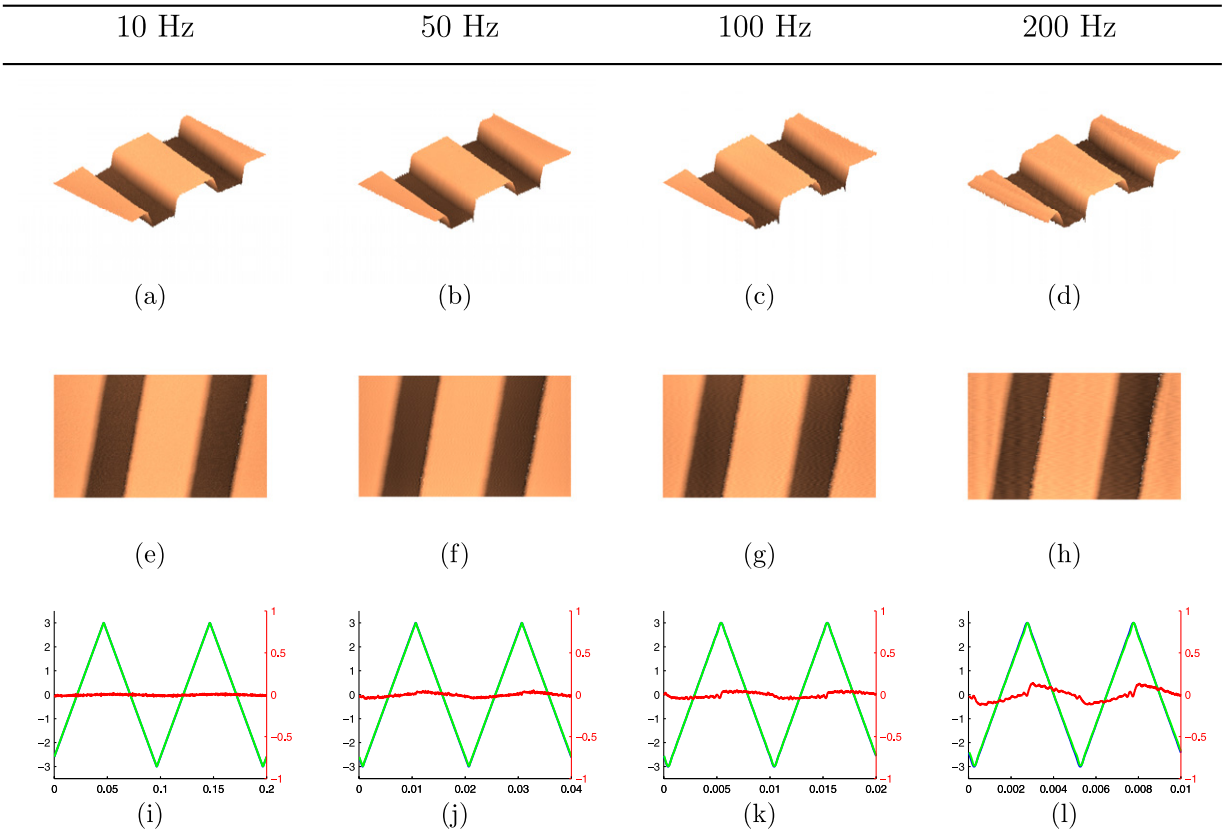

Figure 14. Closed loop scan performance with feedforward of the nanopositioner: blue lines represent the reference signal, green lines indicate the output signals from capacitive sensors converted to equivalent displacement and red lines represent the tracking error.

Table 2. RMS tracking error for a 6 μm scanning range.

	Open loop		Closed loop without FF		Closed loop with FF	
Frequency (Hz)	nm	% of scan range	nm	% of scan range	nm	% of scan range
10	348.5	5.808	15.4	0.256	9	0.15
50	371.2	6.186	67.1	1.118	22.7	0.378
100	415.5	6.925	132.3	2.205	31.6	0.526
200	488.5	8.141	267.8	4.463	61.5	1.025

to (l) show that the tracking performance has improved. However, the presence of time delay still hampers the tracking performance.

When the feedforward control is integrated with feedback control the performance is further improved. No considerable differences are observed in the image quality shown in figures 14(e) to (h). The tracking performance is improved, which is evident from the x-direction signal plots in figures 14(i) to (l). These clearly show that the time delay has been compensated using the feedforward control.

To evaluate the tracking performance of the three cases, i.e. open loop, closed loop and closed loop with feedforward control, table 2 lists the corresponding root mean square error e_{rms} and the percentage error of the total scan range (6 μm).

It is clear from table 2 that with the IRC and integral action in closed loop, good tracking performance is achieved at low speed ($e_{\text{rms}}(\%) = 0.256$ at 10 Hz) compared to the open loop tracking ($e_{\text{rms}}(\%) = 5.808$ at 10 Hz). However, at high speeds the effect of time delay becomes significant and the phase lag contributes greatly to the tracking error ($e_{\text{rms}}(\%) = 4.463$ at 200 Hz). Although the nonlinearities are minimized and vibration effects are suppressed the percentage error is significant. With the combined feedforward and feedback controllers the phase lag is reduced and good tracking ($e_{\text{rms}}(\%) = 1.025$ at 200 Hz) is achieved. The results presented above are comparable to those presented in [21].

9. Conclusions and future work

The field of nanotechnology is progressing, posing multidisciplinary research problems for scientists. High-speed imaging is in demand, which requires expertise in mechanical design for a high-speed nanopositioner and efficient control design to enhance the imaging performance. In this paper, a compact

serial-kinematic nanopositioner built in-house was considered for experimentation. The objective was to achieve high-speed scanning with nanoscale accuracy. The performance of the nanopositioner was hampered by (a) vibrations which are a consequence of the lightly damped resonant structure of the nanopositioner, (b) nonlinearity due to hysteresis from the piezoelectric actuator and (c) time delay due to the capacitive sensor electronics. An IRC was designed to sufficiently damp the resonant mode of the nanopositioner and increase the gain margins. The stability conditions for the IRC were extended to accommodate resonant time delayed systems such as the nanopositioning stage. Integral action and feedforward controllers were designed to improve the tracking performance. Increase in the scanning speed up to 200 Hz was reported. The scanning results show a remarkable improvement in the performance of the nanopositioner with the proposed control strategy. The combined IRC and integral action substantially mitigate the effects of vibration and hysteresis. This system when cascaded with feedforward control further improves the tracking performance of the system by eliminating the time delay. The RMS tracking error values obtained indicate the magnitude of accuracy achieved with this control strategy.

The next bottleneck which limits the scan speed of the AFM is the limited vertical feedback control bandwidth. Future objectives include development and implementation of control to increase the gain margin of the vertical feedback loop for effective feature tracking.

Acknowledgment

The reported research was performed at the Laboratory for Dynamics and Control of Nanosystems at the University of Newcastle, Callaghan, NSW, Australia. This work was supported by the Australian Research Council (ARC).

References

[1] Binnig C F and Quate G 1986 Atomic force microscope *Phys. Rev. Lett.* **56** 930–3
[2] Tsukada M, Kobayashi N, Brandbyge M and Nakanishi S 2000 Physics of artificial nano-structures on surfaces *Surface Interface Anal.* **64** 139–55
[3] Jandt K D, Finke M and Cacciafesta P 2000 Aspects of the physical chemistry of polymers, biomaterials and mineralised tissues investigated with atomic force microscopy (AFM) *Colloids Surfaces* B **19** 301–14
[4] You H X and Yu L 1999 Atomic force microscopy imaging of living cells: progress, problems and prospects *Methods Cell Sci.* **21** 1–17
[5] Burnham N A and Colton R J 1989 Measuring the nanomechanical properties and surface forces of materials using an atomic force microscope *J. Vacuum Sci. Technol.* A **7** 2906–13
[6] Danzebrink H U, Koenders L, Wilkening G, Yacoot A and Kunzmann H 2006 Advances in scanning force microscopy for dimensional metrology *CIRP Ann. - Manuf. Technol.* **55** 841–78
[7] Geim K S and Novoselov A K 2007 The rise of graphene *Nature Mater.* **6** 183–91
[8] Meyer E, Hug H J and Bennewitz R 2004 *Scanning Probe Microscopy: The Lab on a Tip* (Heidelberg: Springer)
[9] Ando T, Uchihashi T, Kodera N, Yamamoto D, Miyagi A, Taniguchi M and Yamashita H 2008 High-speed AFM and nano-visualization of biomolecular processes *Pflügers Arch. Eur. J. Physiol.* **456** 211–25
[10] Meyer G and Amer N M 1988 Novel optical approach to atomic force microscopy *Appl. Phys. Lett.* **53** 1045–7
[11] Rost M J *et al* 2005 Scanning probe microscopes go video rate and beyond *Rev. Sci. Instrum.* **76** (5) 053710
[12] Schitter G and Rost M J 2008 Scanning probe microscopy at video-rate *Mater. Today* **11** (Suppl. 1) 40–8
[13] Rost M J, van Baarle G J C, Katan A J, van Spengen W M, Schakel P, van Loo W A, Oosterkamp T H and Frenken J W M 2009 Video-rate scanning probe control challenges: setting the stage for a microscopy revolution *Asian J. Control* **11** 110–29
[14] Hobbs J K, Vasilev C and Humphris A D L 2006 Video AFM—a new tool for high speed surface analysis *Analyst.* **131** 251–6
[15] Ando T and Kodera N 2012 Visualization of mobility by atomic force microscopy *Intrinsically Disordered Protein Analysis, (Methods in Molecular Biology)* vol 896 (New York: Springer) pp 57–69
[16] Porat B 1997 *A Course in Digital Signal Processing* (New York: Wiley)
[17] Abramovitch D Y, Andersson S B, Pao L Y and Schitter G 2007 A tutorial on the mechanisms, dynamics, and control of atomic force microscopes *ACC: Proc. American Control Conf. (ACC)* pp 3488–502
[18] Devasia S, Eleftheriou E and Moheimani S O R 2007 A survey of control issues in nanopositioning *IEEE Trans. Control Syst. Technol.* **15** 802–23
[19] Moheimani S O R 2008 Invited review article: accurate and fast nanopositioning with piezoelectric tube scanners: emerging trends and future challenges *Rev. Sci. Instrum.* **79** 071101
[20] Schitter G, Astrom K J, DeMartini B E, Thurner P J, Turner K L and Hansma P K 2007 Design and modeling of a high-speed AFM-scanner *IEEE Trans. Control Syst. Technol.* **15** 906–15
[21] Kenton B J and Leang K K 2012 Design and control of a three-axis serial-kinematic high-bandwidth nanopositioner *IEEE/ASME Trans. Mechatronics* **17** 356–69
[22] Yong Y K and Moheimani S O R 2010 A compact XYZ scanner for fast atomic force microscopy in constant force contact mode *AIM: Proc. IEEE/ASME Int. Conf. Advanced Intelligent Mechatronics* (July)
[23] Yong Y K, Aphale S S and Moheimani S O R 2009 Design, identification and control of a flexure-based XY stage for fast nanoscale positioning *IEEE Trans. Nanotechnol.* **8** 46–54
[24] Wadikhaye S P, Yong Y K and Moheimani S O R 2011 A novel serial-kinematic AFM scanner: design and characterization *IECON: Proc. 37th Annual Conf. on IEEE Industrial Electronics Society* pp 50–5
[25] Leang K K and Fleming A J 2009 High-speed serial-kinematic SPM scanner: design and drive considerations *Asian J. Control* **11** 144–53
[26] Yong Y K, Bhikkaji B and Moheimani S O R 2013 Design, modeling and FPAA-based control of a high-speed atomic force microscope nanopositioner *IEEE/ASME Trans. Mechatronics* **18** 1060–71
[27] Wadikhaye S P, Yong Y K and Moheimani S O R 2012 Design of a compact serial-kinematic scanner for high-speed atomic force microscopy: an analytical approach *Micro Nano Lett.* **7** 309–13
[28] Ratnam M, Bhikkaji B, Fleming A J and Moheimani S O R 2005 PPF control of a piezoelectric tube scanner *CDC-ECC: 44th IEEE Conf. on Decision and Control and European Control Conference* pp 1168–73

[29] Fleming A J and Moheimani S O R 2006 Sensorless vibration suppression and scan compensation for piezoelectric tube nanopositioners *IEEE Trans. Control Syst. Technol.* **14** 33–44
[30] Halim D and Moheimani S O R 2001 Spatial resonant control of flexible structures: application to a piezoelectric laminate beam *IEEE Trans. Control Syst. Technol.* **9** 37–53
[31] Aphale S S, Devasia S and Moheimani S O R 2008 High-bandwidth control of a piezoelectric nanopositioning stage in the presence of plant uncertainties *Nanotechnology* **19** 125503
[32] Bhikkaji B, Ratnam M, Fleming A J and Moheimani S O R 2007 High-performance control of piezoelctric tube scanners *IEEE Trans. Control Syst. Technol.* **15** 853–66
[33] Bhikkaji B, Moheimani S O R and Petersen I R 2008 Multivariable integral control of resonant structures *CDC: Proc. 47th IEEE Conf. on Decision and Control*
[34] Bhikkaji B and Moheimani S O 2008 Integral resonant control of a piezoelectric tube actuator for fast nanoscale positioning *IEEE/ASME Trans. Mechatronics* **13** 530–7
[35] Fleming A J 2010 Nanopositioning system with force feedback for high-performance tracking and vibration control *IEEE/ASME Trans. Mechatronics* **15** 433–47
[36] Abramovitch D Y, Hoen S and Workman R 2008 Semi-automatic tuning of PID gains for atomic force microscopes *ACC: Proc. American Control Conference* pp 2684–9
[37] Aphale S S, Fleming A J and Moheimani S O R 2007 Integral resonant control of collocated smart structures *Smart Mater. Struct.* **16** 439–46
[38] Pereira E, Aphale S S, Feliu V and Moheimani S O R 2011 Integral resonant control for vibration damping and precise tip-positioning of a single-link flexible manipulator *IEEE/ASME Trans. Mechatronics,* **16** 232–40
[39] Aphale S S, Ferreira A and Moheimani S O R 2013 A robust loop-shaping approach to fast and accurate nanopositioning *Sensors Actuators* A **204** 88–96
[40] Lee C and Salapaka S M 2009 Robust broadband nanopositioning: fundamental trade-offs, analysis, and design in a two-degree-of-freedom control framework *Nanotechnology* **20** 035501
[41] Dong J, Salapaka S M and Ferreira P M 2008 Robust control of a parallel-kinematic nanopositioner *J. Dyn. Syst., Meas., Control* **130** 041007
[42] Tuma T, Lygeros J, Kartik V, Sebastian A and Pantazi A 2012 High-speed multiresolution scanning probe microscopy based on lissajous scan trajectories *Nanotechnology* **23** 185501
[43] Kotsopoulos A, Pantazi A and Antonakopoulos T 2010 Control for high-speed archimedean spiral nanopositioning *ICECS: Proc. 17th IEEE Int. Conf. on Electronics, Circuits, and Systems* pp 998–1001
[44] Liaw H C, Shirinzadeh B and Smith J 2008 Sliding-mode enhanced adaptive motion tracking control of piezoelectric actuation systems for micro/nano manipulation *IEEE Trans. Control Syst. Technol.* **16** 826–33
[45] Bashash S and Jalili N 2009 Robust adaptive control of coupled parallel piezo-flexural nanopositioning stages *IEEE/ASME Trans. Mechatronics* **14** 11–20
[46] Li Y and Xu Q 2010 Adaptive sliding mode control with perturbation estimation and PID sliding surface for motion tracking of a piezo-driven micromanipulator *IEEE Trans. Control Systems Technol.* **18** 798–810
[47] Petersen I R and Lanzon A 2010 Feedback control of negative-imaginary systems *IEEE Control Syst. Mag.* 54–72
[48] Lanzon A and Patra S 2011 Stability analysis of interconnected systems with 'mixed' negative-imaginary and small-gain properties *IEEE Trans. Autom. Control* **56** 1395–400
[49] Abe N and Yamanaka K 2003 Smith predictor control and internal model control tutorial *SICE 2003 Annual Conf.* vol 2, pp 1383–7
[50] Clayton G M, Tien S, Leang K K, Zou Q and Devasia S 2009 A review of feedforward control approaches in nanopositioning for high-speed SPM *J. Dyn. Syst., Meas., Control* **131** 061101
[51] Leang K K and Devasia S 2007 Feedback-linearized inverse feedforward for creep, hysteresis, and vibration compensation in AFM piezoactuators *IEEE Trans. Control Syst. Technol.* **15** 927–35
[52] Polit S and Dong J 2009 Design of high-bandwidth high-precision flexure-based nanopositioning modules *J. Manuf. Syst.* **28** 71–7
[53] Cardarelli F 2000 *Materials Handbook: A Concise Desktop Reference* (Berlin: Springer)
[54] Mckelvey T, Fleming A and Moheimani S O R 2000 Subspace based system identification for acoustic enclosure *Proc. 2000 IEEE Int. Conf. on Control Application*
[55] Lanzon A and Petersen I R 2008 Stability robustness of a feedback interconnection of systems with negative imaginary frequency response *IEEE Trans. Autom. Control* **53** 1042–6
[56] Devasia S 2002 Should model-based inverse inputs be used as feedforward under plant uncertainties? *IEEE Trans. Autom. Control* **47** 1865–71
[57] Fleming A J and Wills A G 2009 Optimal periodic trajectories for band-limited systems *IEEE Trans. Control Syst. Technol.* **17** 552–62